Journal of Materials Science & Technology 166 (2023) 145–154

Contents lists available at ScienceDirect

Journal of Materials Science & Technology

journal homepage: www.elsevier.com/locate/jmst

Research Article

Outstanding specific yield strength of a refractory high-entropy composite at an ultrahigh temperature of 2273 K

Bo Sun[a,b], Jinyong Mo[a], Qianqian Wang[b], Yongxiong Chen[a], Zhibin Zhang[a], Baolong Shen[b,*], Xiubing Liang[a,*]

[a] Defense Innovation Institute, Academy of Military Science, Beijing, 100071, China
[b] School of Materials Science and Engineering, Jiangsu Key Laboratory for Advanced Metallic Materials, Southeast University, Nanjing, 211189, China

ARTICLE INFO

Article history:
Received 23 February 2023
Revised 14 May 2023
Accepted 23 May 2023
Available online 13 June 2023

Keywords:
Refractory high-entropy composite
Metastability
Ultrahigh temperature
Mechanical property
Phase transformation

ABSTRACT

We reported on the mechanical properties and microstructural evolution of a $W_{20}Ta_{30}Mo_{20}C_{30}$ (at.%) refractory high-entropy composite (RHEC). The RHEC exhibited outstanding yield strength at both 2273 and 1873 K. Microstructural investigations revealed that the as-cast RHEC had a triple-phase structure consisting of FCC dendrites, HCP matrix, HCP-BCC eutectic structure, and FCC-BCC eutectoid structure, and exhibited high-density defects owing to the complex phase transformations during solidification. After annealing at 2273 K, the precipitation of the BCC phase from the FCC dendrites and the decomposition of the HCP phase into the FCC-BCC eutectoid structure was observed to significantly refine the grain sizes of all triple phases. After compression at 2273 K, the ceramic phases and solid solution precipitated out from each other, which helps to avoid persistent softening after the yielding of RHEC. Further analyses suggested that the dominant deformation mechanisms of the BCC phase and HCP phase are dislocation glide and transformation-induced plasticity; whereas those of the FCC phase are twinning- and transformation-induced plasticity. The outstanding yield strength of this RHEC at ultrahigh temperatures may originate from the high-content ceramic phases and the structural metastability of the multi-principal composition. These findings provide a novel strategy to design RHECs by alloying high-content nonmetallic elements, which contributes to further breaking through their performance limits at ultrahigh temperatures.

1. Introduction

High strength and excellent softening resistance at elevated temperatures are essential for some hot-end structural materials that are used in extreme environments, like aerospace vehicles and reusable rocket technologies [1–3]. Nickel-based superalloys are the most commonly used materials for high-temperature applications in the past decades. However, the superalloys would suffer from severe softening effects at temperatures above 1473 K. Therefore, the development of new materials with a superior mechanical performance at ultrahigh temperatures becomes imperative [4]. Refractory high-entropy alloys (RHEAs), consisting of several principal refractory elements to constitute the solid-solution phase, have been developed since 2010 [5]. Among many RHEAs, the WTaMoNb system alloys have shown outstanding softening resistance and excellent structural stability at 1473–1873 K [6] and hence are considered one of the most promising materials for ultrahigh-temperature applications [7].

In the past decade, many efforts have been devoted to enhancing the mechanical properties of WTaMoNb system RHEAs at ultrahigh temperatures by alloying with metallic elements [8–10]. For instance, alloying with ductile elements (e.g., Ti) simultaneously improved the strength and plasticity at temperatures below 1500 K [8]. However, the resulting reduction in melting point led to an inevitable decrease in compressive strength to 218 MPa at 1873 K for WTaMoNbTi RHEA [9]. Wan et al. [10] prepared WReTaMo RHEA to increase the melting point of the RHEA, however, they found that the replacement of Nb with *Re* can deteriorate the strength at 1873 K due to the decreased structural stability at grain boundaries (GBs). These studies have demonstrated that the compositional modification by adjusting metal elements can not significantly increase the strength at ultrahigh temperatures. To date, the WTaMoNb RHEA still exhibits the most promising mechanical properties at 1873 K among the existing RHEAs [6].

Recent studies have shown that the addition of nonmetallic elements into RHEAs may be a promising method to further improve

* Corresponding authors.
E-mail addresses: blshen@seu.edu.cn (B. Shen), liangxb_d@163.com (X. Liang).

https://doi.org/10.1016/j.jmst.2023.05.014
1005-0302/

the mechanical properties at ultrahigh temperatures [11–15]. The introduction of a low amount (e.g., below 1 at.%) of nonmetallic elements (B or C) can enhance the interstitial solid-solution effect and avoid the segregation of impurity at GBs, which contributes to a remarkable improvement in room-temperature plasticity with only slight reduction in high-temperature strength [11]. More interestingly, the addition of a larger amount of nonmetallic elements (e.g., 5 at.%–20 at.%) allows the formation of multi-component ceramic phases to form refractory high-entropy composites (RHECs), which not only increases the high-temperature strength but also reduces the density [12,13]. For example, the as-cast $C_xHf_{0.25}NbTaW_{0.5}$ (x = 0–0.25) RHECs showed an evident increase in yield strength at both room temperature (280 MPa) and 1673 K (294 MPa) with the addition of ~8.3 at.% C [13]. Our previous work has reported that the 10 at.% N alloyed HfNbTaTiV RHEA exhibited an excellent combination of high yield strength (of 639 MPa) at 1473 K and relatively low density of 10.56 g cm^{-3}, and demonstrated that the multi-component ceramic phase showed instability prior to the solid solution phase as the serving temperature increased to 1673 K [14]. Besides, Wei et al. [15] designed a eutectic-structured $Re_{0.5}MoNbW(TaC)_{0.9}$ RHEC via alloying ~17 at.% C, which can retain the yield strength from 1440 MPa at room temperature to 1080 MPa at 1473 K, displaying excellent softening resistance at elevated temperatures. However, limited research has been focused on RHECs with alloying high-content nonmetallic elements (over 20 at.%), which may further break through the strength limits at ultrahigh temperatures. More importantly, the mechanical properties and microstructure evolution at temperatures above 1873 K remain unexplored.

In this work, we designed an RHEC by alloying with a high amount (30 at.%) of C and reported its mechanical properties at an ultrahigh-temperature of 2273 K. Then we investigated the underlying mechanisms of structural metastability of the RHEC and the corresponding influences on its ultrahigh-temperature mechanical properties by detailed microstructural characterization. This work provides a novel strategy to design RHECs by alloying high-content nonmetallic elements, which not only enhanced the strength at ultra-high temperatures but also reduced the density (both critical for their potential engineering applications).

2. Materials and methods

Ingots with a nominal composition of $W_{20}Ta_{30}Mo_{20}C_{30}$ (at.%) were prepared by vacuum arc melting with W, Mo, and TaC (purity ≥ 99.95 wt.%) under a protective argon atmosphere. The ingots were remelted at least six times to ensure compositional homogeneity. Compression tests were conducted at 2273 K under pure argon in a vacuum furnace with a Zwick KAPPA 100 dynamic thermal simulation testing machine, and the as-cast samples with a diameter of 2 mm and a height of 4 mm were used. The cylinder sample was firstly soaked for 10 min after heating to 2273 K, then compressed with the strain rate of 10^{-3} s^{-1}, and finally cooled in the furnace. The experimental details of compression tests at ultrahigh temperatures were provided in the supplementary materials (Text 1). Simultaneously, another as-cast ingot was placed aside the cylinder sample to perform the annealing process (with the same heating, soaking, and cooling duration) without deformation. The microstructure of the as-cast, deformed at 2273 K, and undeformed at 2273 K (i.e., annealed) samples (hereinafter denoted as samples AC, DF2273, UDF2273) were thoroughly characterized by X-ray diffraction (XRD, Bruker D8 Discover), scanning electron microscope (SEM, FEI Nova Nano 450) equipped with back-scattering electron (BSE), electron back-scattering diffraction (EBSD, FEI Sirion) and transmission electron microscope (TEM, Talos F200X, and FEI G2 20). The scanning rate of XRD tests was 4° min^{-1}. The EBSD samples were polished by a vibratory polisher (Buehler Vibromet 2) with nanoscale SiO_2 suspension for 6 h in medium frequency mode and tested with a step size of 0.3 μm. The TEM samples were thinned by an ion beam thinner (GATAN-M691).

Phase diagrams of $W_{20}Ta_{30}Mo_{20}C_{30}$ RHEC were calculated using the Thermo-calc software and the TCHEA database [16–18]. The thermodynamic equilibrium phase diagram and phase transformations were predicted based on the Gibbs energy minimization for a given multi-principal composition. Besides, the classical Scheil solidification simulation was performed to account for the non-equilibrium microstructure on the assumption that the diffusion in the liquid phase was sufficient while that in the solid can be negligible.

3. Results

3.1. Microstructure at the as-cast state

Fig. 1 shows the as-cast microstructure of $W_{20}Ta_{30}Mo_{20}C_{30}$ RHEC measured by XRD and EBSD. As shown in Fig. 1(a), sample AC exhibits a ternary-phase structure composed of the FCC phase, HCP phase, and BCC phase. Fig. 1(b, c) shows the phase distribution and orientation map, respectively. The FCC phase has a dendritic morphology on the HCP matrix, and the BCC phase is distributed in both the HCP and FCC phases. All three phases show obvious solidification texture (Fig. S2 and Text 2 in Supplementary Information), and the HCP phase shows the highest intensity of 22.70 m.u.d. (multiple uniform distribution) in the pole figures (PFs) with a strong ⟨0001⟩ // z texture. The phase fraction is given in Fig. 2(a), and the relative ratio of FCC, HCP, and BCC is approximately 4:5:1 in sample AC. Fig. 1(d) shows the distribution of phase boundaries (PBs). It can be found that there are some FCC dendrites with dense PBs as indicated by the red square, which implies that solid-state phase transformation may occur in the primary FCC phase during the subsequent solidification process. As shown in Figs. 1(e) and 2(b), the FCC phase has the largest grain size due to the presence of dendrites. As shown in Fig. 1(f), the distribution of the Kernel average misorientation (KAM) angle is significantly different in the three phases, and the average value of KAM angle ($KAM_{ave.}$) in the BCC phase is much higher than that in both the HCP and FCC phase. The density of geometrically necessary dislocations (GNDs) can be estimated by strain-gradient theory (i.e., $\rho_{GND} = 2\theta/\mu b$ [19,20], where ρ_{GND}, θ, μ, and b represent the GND density (m^2), misorientation angle ($KAM_{ave.}$, deg.), step size (0.3 μm) and Burgers vector (nm), respectively). All three phases have high ρ_{GND}, and the ρ_{GND} values of the HCP phase and BCC phase are much higher than that of the FCC phase.

In order to analyze the solidification behavior of the triple-phase structure of $W_{20}Ta_{30}Mo_{20}C_{30}$ RHEC, the simulation of thermodynamic phase diagrams was conducted and the results are presented in Fig. 3. As shown in Fig. 3(a), the equilibrium phase diagram suggests that the RHEC has complex phase transformations during solidification. There are seven solidification stages including four liquid-solid stages (LS-1 to LS-4) and three solid-solid stages (SS-5 to SS-7). The corresponding phase transformation reactions are given in Table 1. Fig. 3(b) presents the element content in the liquid phase derived by Fig. 3(a). It can be found that the formation of a single FCC phase (LS-1) or a single HCP phase (LS-2 and LS-3) consumes high-content C, which indicates the FCC and HCP phases are multi-component carbides, i.e., ceramic phase [12]. On the contrary, the BCC phase is a solid solution. The Scheil solidification simulation is exhibited in Fig. 3(c) to account for the as-cast microstructure of RHEC that is away from equilibrium solidification. Obviously, LS-1 is similar between the equilibrium and Scheil solidification, but the back diffusion of FCC (LS-2) hardly occurs in the latter. Thus, a more liquid phase can be reserved to pro-

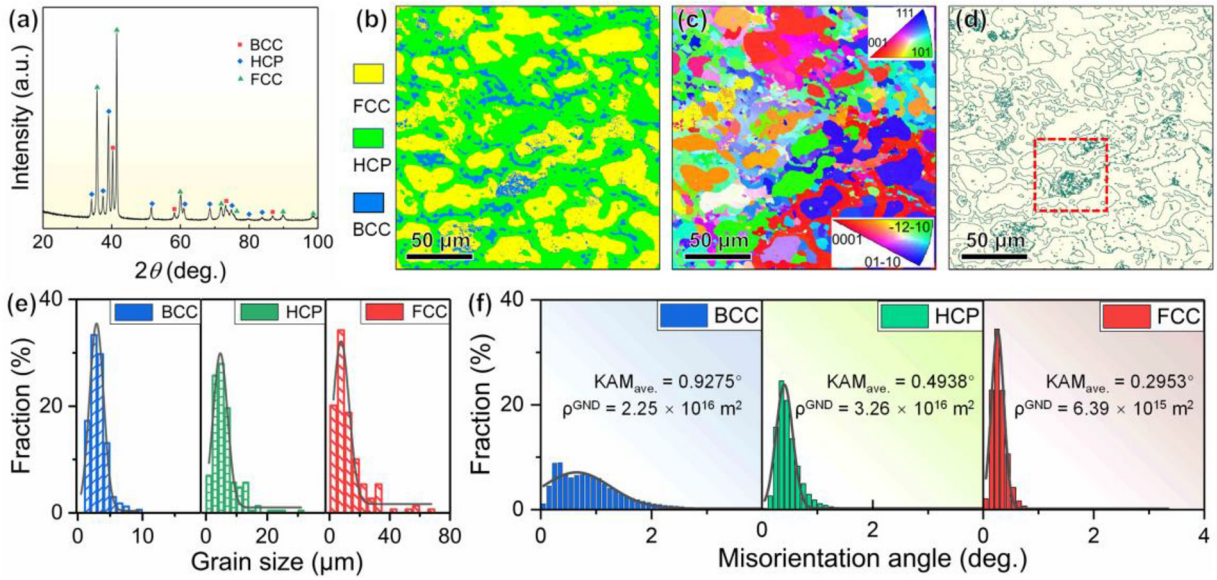

Fig. 1. Microstructure of the sample AC. (a) XRD pattern; (b) phase distribution; (c) orientation map; (d) phase boundary distribution; (e) grain size distribution; (f) KAM value distribution with KAM_{ave} value and ρ_{GND} value.

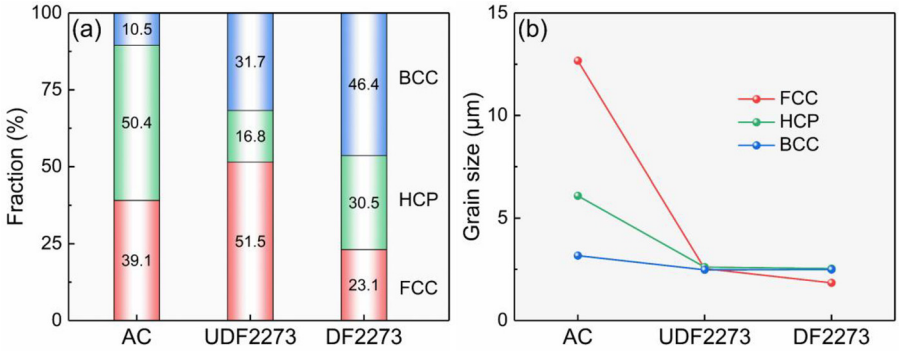

Fig. 2. (a) Phase composition and (b) grain size values of samples AC, UDF2273, and DF2273.

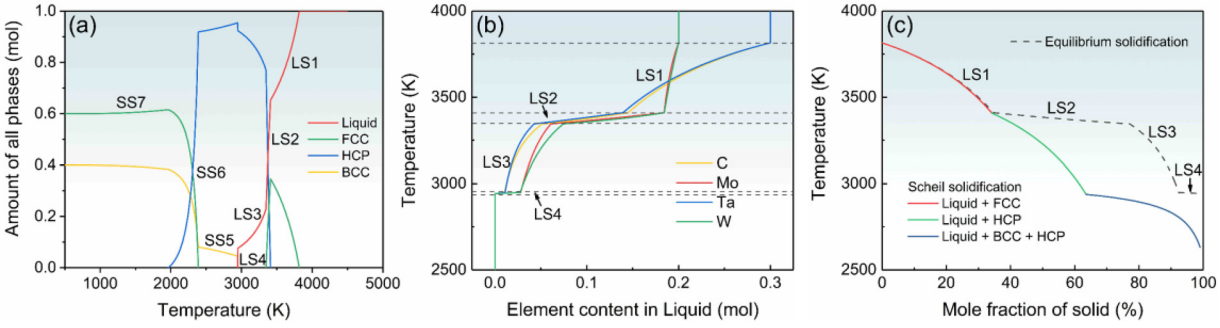

Fig. 3. Thermodynamic phase diagrams of the $W_{20}Ta_{30}Mo_{20}C_{30}$ RHEC. (a) equilibrium phase diagram; (b) element content in liquid phase; (c) Scheil solidification simulation.

mote the formation of the HCP phase and eutectic structure (LS-3). It should be noted that the temperature at the end of the liquid phase (terminal temperature of LS-4) in Scheil solidification is much lower than that in equilibrium solidification, suggesting the subsequent solid-solid phase transformations may be postponed.

TEM analysis was carried out to further investigate the solidification microstructure of sample AC, and the results are presented in Fig. 4. A high density of intersecting stacking faults (SFs), as indicated by the yellow arrows in Fig. 4(a), can be observed in the bright field (BF) image of the FCC dendrite (corresponding to LS-1). The starburst line (as indicated by the red arrows) in the selected area electron diffraction (SAED) image in Fig. 4(b) demonstrates that the SFs are located in $\{111\}_{FCC}$ planes. Meanwhile, only a small number of short dislocations (as indicated by the green arrows) can be found in the FCC phase. As shown in Fig. 4(c), the dense parallel dislocations reveal that some slip systems on the basal planes of the HCP phase are activated. Fig. 4(d, e) exhibits the SAED patterns of the HCP phase, demonstrating that the HCP phase is a long-period ordered phase with special atomic sites due to the presence of the superlattice (see the green circle) on the prismatic plane $(2\bar{1}\bar{1}0)$ rather than $(10\bar{1}0)$. Fig. 4(f) shows the dark field (DF) image of the lamellar eutectic structure (corresponding

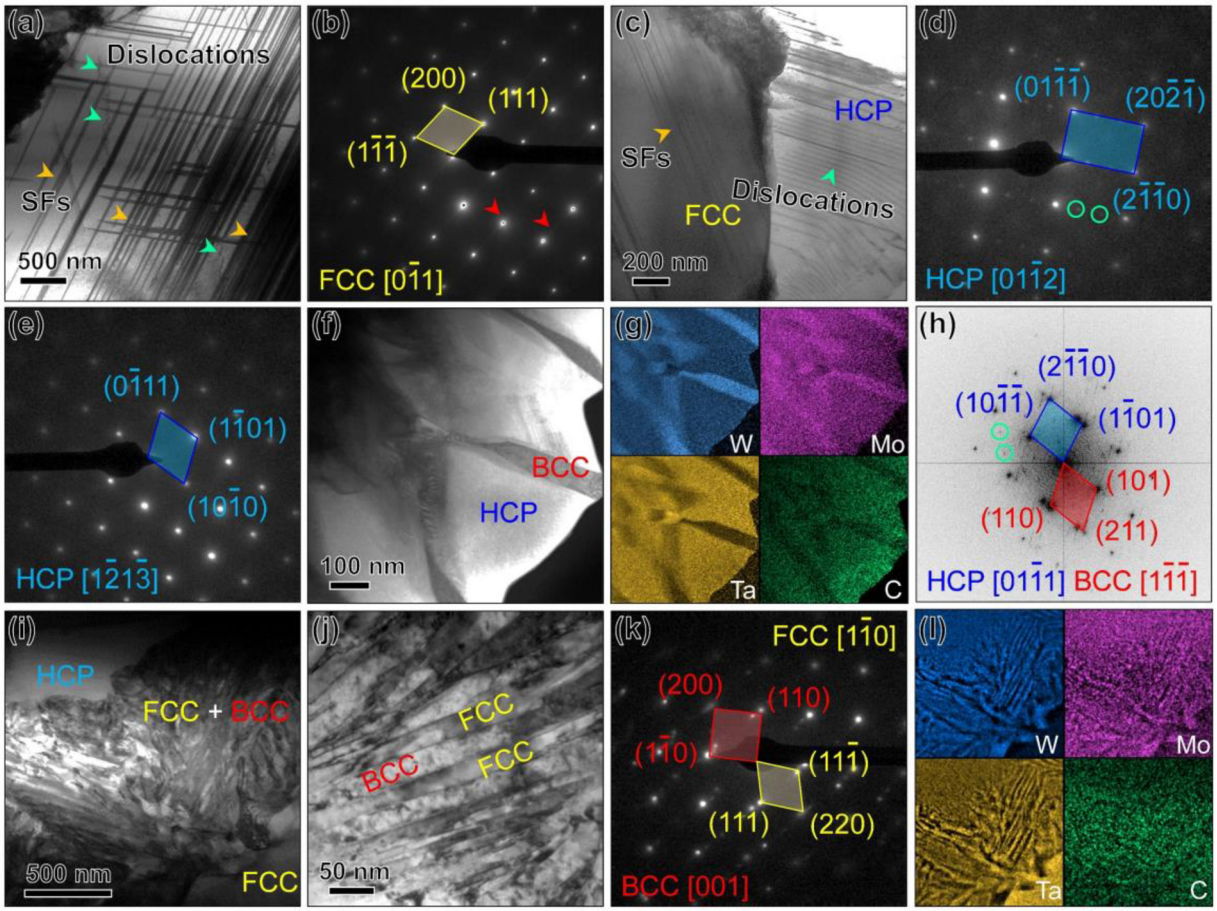

Fig. 4. TEM analysis of the sample AC. (a) BF image and (b) SAED pattern of the FCC phase; (c) BF image and (d, e) SAED patterns of the HCP phase; (f) DF image, (g) elemental distribution and (h) SAED pattern of the HCP-BCC eutectic structure; (i) DF image, (j) enlarged BF image, (k) SAED pattern and (l) elemental distribution of the FCC-BCC eutectoid structure.

Table 1
Phase transformation stages of $W_{20}Ta_{30}Mo_{20}C_{30}$ RHEC.

Type	Stage	Phase transformation
Liquid-solid	LS-1	Liquid → FCC
	LS-2	Liquid + FCC → HCP
	LS-3	Liquid → HCP
	LS-4	Liquid → HCP + BCC
Solid-solid	SS-5	HCP → BCC
	SS-6	HCP → FCC + BCC
	SS-7	FCC → BCC

to LS-4) where embedded in the HCP matrix. Fig. 4(g, h) exhibits the elemental distribution of the eutectic structure and the SAED pattern at PB, respectively. The bright lamella of the eutectic structure is Ta- and C-rich and identified as an ordered HCP phase while the dark lamella is W- and Mo-rich and identified as a disordered BCC phase. In order to evaluate the boundary relationship, the mismatching degree ($\delta^{(hkl)_s}_{(hkl)_n}$) was calculated by Bramfitt's lattice misfit method [21]

$$\delta^{(hkl)_s}_{(hkl)_n} = \sum_{i=1}^{3} \frac{\left|\left(d_{[uvw]^i_s}\cos\theta\right) - d_{[uvw]^i_n}\right|}{d_{[uvw]^i_n}} \times 100$$

where d represents the planar spacing and θ is the included angle between the $[uvw]_s$ and $[uvw]_n$. The mismatching degree between the HCP and BCC phases is 5.6%, indicating the formation of semi-coherent PBs in the HCP-BCC eutectic structure. Fig. 4(l, j) shows a DF image and an enlarged BF image of the lamellar eutectoid structure (corresponding to SS-6). The eutectoid structure is located between the FCC dendrites and the HCP matrix with an average lamellar thickness of ~20 nm. The eutectoid structure is composed of a Ta- and C-rich FCC phase and a W- and Mo-rich BCC phase, which are identified by the SAED pattern at PB and the elemental distribution in Fig.4(k, l), respectively. Besides, the mismatching degree between the two phases is 6.4%, which suggests that semi-coherent PBs are also formed in the FCC-BCC eutectoid structure.

3.2. Ultrahigh-temperature mechanical properties

Figure 5(a) shows the engineering stress-strain curve of $W_{20}Ta_{30}Mo_{20}C_{30}$ RHEC at 2273 K. It exhibits an initial yielding followed by a stress drop of ~80 MPa at a strain of ~7%, and then the stress remains nearly constant (~150 MPa) with further increasing strain to ~30% followed by gradual softening. The yield strength ($\sigma_y^{2273\ K}$) and ultimate strength ($\sigma_m^{2273\ K}$) are 222 ± 22 and 234 ± 23 MPa, respectively, and the fracture strain is over 40%.

Considering no mechanical property at 2273 K has been reported in high-entropy materials, the compression tests of $W_{20}Ta_{30}Mo_{20}C_{30}$ RHEC were additionally performed at 1873 K for comparison with the available data of other RHEAs/RHECs. As shown in Fig. 5(a), the $\sigma_y^{1873\ K}$ and $\sigma_m^{1873\ K}$ of the $W_{20}Ta_{30}Mo_{20}C_{30}$ RHEC are 1257 ± 70 and 1890 ± 116 MPa, respectively. For comparison, yield strength and specific yield strength (σ_y/ρ) as a function of testing temperatures of $W_{20}Ta_{30}Mo_{20}C_{30}$ RHEC together

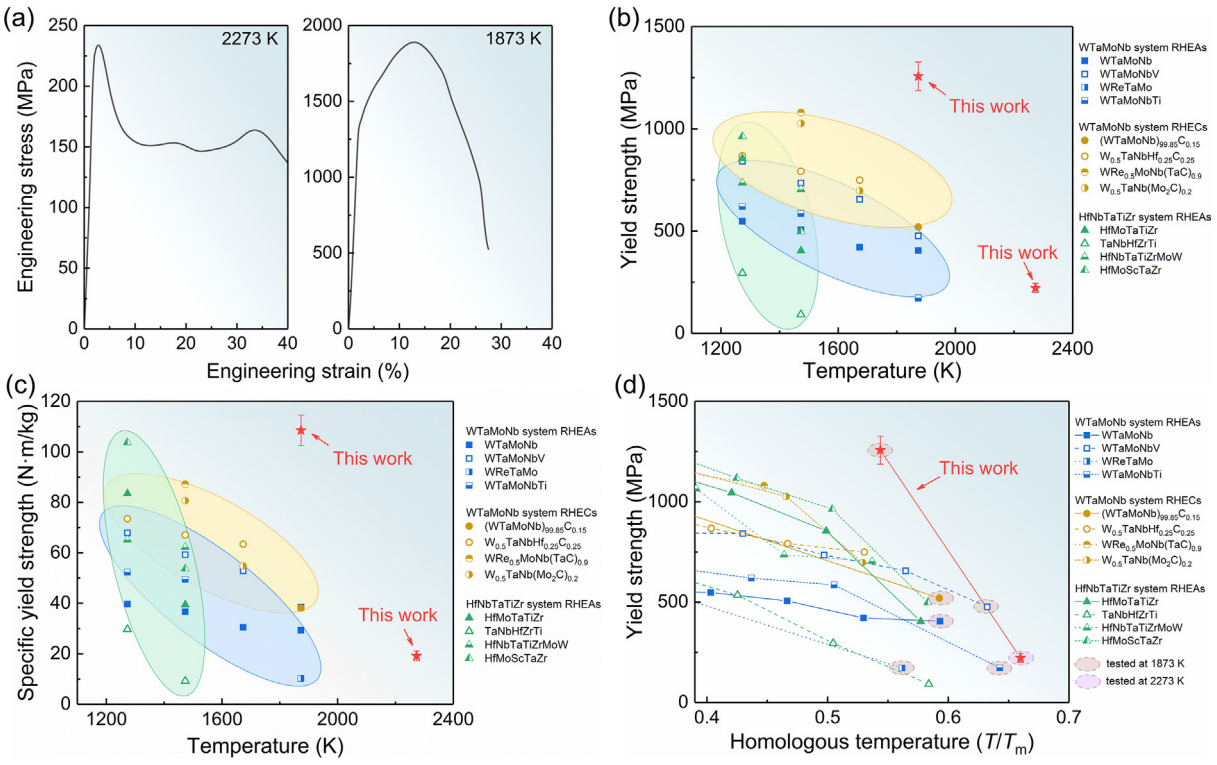

Fig. 5. Ultrahigh-temperature mechanical properties of $W_{20}Ta_{30}Mo_{20}C_{30}$ RHEC. (a) engineering stress-strain curves at 2273 and 1873 K; (b, c) yield strength and specific yield strength as a function of testing temperature; (d) yield strength as a function of homologous temperature (T/T_m) of this work in comparison with other RHEAs/RHECs.

with typical RHEAs/RHECs are plotted in Fig. 5(b, c), where ρ (g cm^{-3}) is the density that calculated by the rule-of-mixture approach [22]. The density of $W_{20}Ta_{30}Mo_{20}C_{30}$ RHEC is relatively low (11.58 g cm^{-3}), and both the yield strength and the specific yield strength of $W_{20}Ta_{30}Mo_{20}C_{30}$ RHEC at 1873 K (108 ± 6 N m kg^{-1}) is much higher than other RHEAs or RHECs [6,8–11,13,15,23–27]. Although the strength of $W_{20}Ta_{30}Mo_{20}C_{30}$ RHEC pronouncedly drops at 2273 K, it remains higher than that of some RHEAs at 1873 K (e.g., WReTaMo [10] and WTaMoNbTi [9]). Besides, as shown in Fig. 5(d), the diagram of the yield strength as a function of homologous temperature (the ratio of test temperature to melting point) further demonstrates the superior mechanical properties of $W_{20}Ta_{30}Mo_{20}C_{30}$ RHEC with a much higher serving temperature.

3.3. Microstructure after annealing at 2273 K

The microstructure of sample UDF2273 was characterized by XRD, BSE-SEM, and EBSD to uncover that the annealing process (at 2273 K, without deformation) altered the microstructure of the $W_{20}Ta_{30}Mo_{20}C_{30}$ RHEC. The XRD pattern (Fig. 6(a)) indicates that sample UDF2273 has the same phase structures as sample AC. However, precipitation phases appear in both the dendrite and the interdendritic, as shown in the BSE-SEM image (Fig. 6(b)), indicating that phase transformations occurred during the annealing treatment. Fig. 6(c, d) is the phase distribution and orientation map of sample UDF2273, respectively. It can be found that the area of FCC dendrites is enlarged and the BCC phase (instead of the HCP phase) becomes the matrix at the interdendritic. As shown in Fig. 2(a), the fraction of the HCP phase in sample UDF2273 decreases while the fractions of the FCC phase and BCC phase increase, suggesting that the annealing treatment promoted the decomposition of the HCP phase (SS-6). The microtexture was weakened after annealing treatment (Fig. S2) and the FCC grains are significantly refined from 12.67 to 2.54 μm (Fig. 2(b)). The grain refinement of sample UDF2273 is induced by phase transformations in the dendritic and interdendritic regions, as evidenced by the dense PBs at all triple phases (Fig. 6(e)). Interestingly, a large amount of Σ3 GBs appears in the FCC phase, as shown by the red lines in Fig. 6(f). The diagram of the misorientation versus distance across the red lines i.e., Fig. 6(g), shows 60° misorientation at the Σ3 GBs. Meanwhile, Fig. 6(h) exhibits the misorientation axis orientations in crystal coordinates (MOCC) images of the FCC phase at 55°–65°, and shows a higher density distribution of lattice rotation at $\{111\}_{FCC}$ in sample UDF2273 than in sample AC, which demonstrates a large number of twin boundaries (TBs) were generated during the annealing process.

TEM analysis was carried out on the sample UDF2273 to further understand the microstructure evolution after the annealing process. Fig. 7(a) exhibits the BF image of the precipitation in the FCC dendrites. As shown in Fig. 7(b, c), the precipitation in the FCC phase is enriched in W and Mo and is identified as the BCC phase. Many intersecting SFs can be found at the end of the BCC precipitation, as indicated by the white circles in Fig. 7(d), suggesting that the phase transformation in FCC dendrites may be related to the reaction of SFs. As shown in Fig. 7(e), some regions with the coexistence of nanoscale FCC and BCC grains are also found in the FCC dendrites. Meanwhile, an annealing twin is observed in the enlarged view and identified by the SAED pattern at TB, as shown in Fig. 7(f, g), respectively. This indicates that the grain refinement of the FCC phase is induced not only by phase transformation but also by annealing twins. Moreover, there is a large area of the eutectoid structure, as shown in Fig. 7(h), demonstrating that the annealing treatment promoted the decomposition of the HCP phase to the FCC and BCC phases (corresponding to SS-6). Hence, it can be concluded that the ceramic phases, i.e., the FCC and HCP phases, are metastable at 2273 K.

3.4. Microstructure after deformation at 2273 K

To understand the microstructure of $W_{20}Ta_{30}Mo_{20}C_{30}$ RHEC after compression at 2273 K, the sample DF2273 was analyzed by XRD and EBSD and the results were presented in Fig. 8. As shown

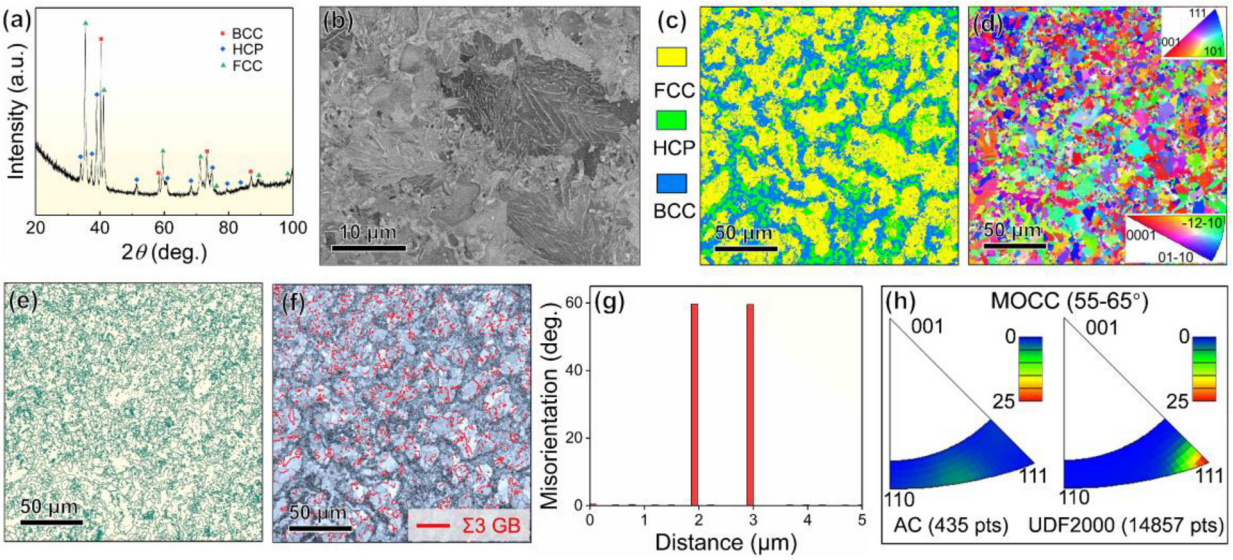

Fig. 6. Microstructure of the sample UDF2273. (a) XRD pattern; (b) BSE-SEM image; (c) phase distribution; (d) orientation map; (e) phase boundary distribution; (f) Σ3 GBs distribution; (g) misorientation across though the Σ3 GBs; (h) misorientation axis distribution in crystal coordinates (MOCC) images.

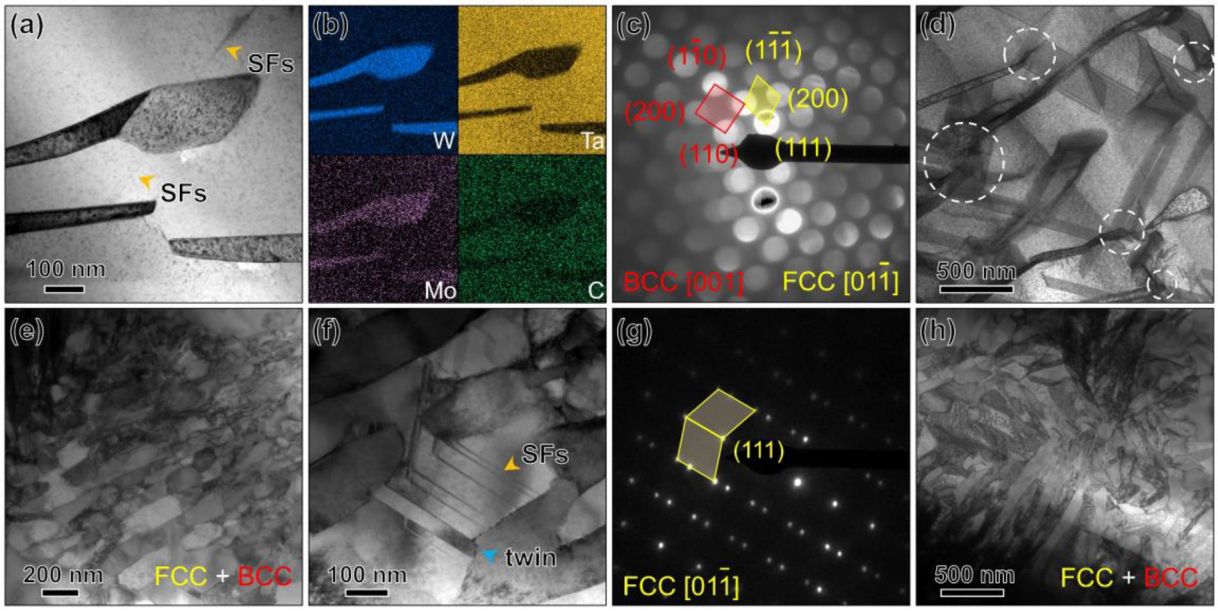

Fig. 7. TEM analysis of the sample UDF2273. (a) BF image, (b) elemental distribution and (c) nano-beam electron diffraction pattern at PB; (d) the interaction between the BCC precipitation and SFs in the FCC dendrite; (e) refined grains in the FCC dendrite; (f) enlarged view of the image (e); (g) SAED pattern at TB; (h) FCC-BCC eutectoid structure.

in Fig. 8(a), the phase structure of sample DF2273 is comprised of FCC phase, HCP phase, and BCC phase, which reveals that no new phase appears after deformation at 2273 K. However, the phase distribution (Fig. 8(b)) shows the morphology of all triple phases becomes more fragmented with a reduced fraction of the FCC phase and an increased fraction of both the HCP and BCC phases, as compared with those after annealing (Fig. 2(a)). Further comparison between the samples DF2273 with UDF2273 reveals that the deformation promotes more phase transformations. After deformation at 2273 K, the microtexture in the FCC and HCP phase was further weakened while it was slightly strengthened in the BCC phase (Fig. S2). Besides, the grain size of the FCC phase is further refined to 1.84 μm, while the average grain sizes of the HCP and BCC phases are comparable to those of sample UDF2273 (Fig. 2(b)). Fig. 8(d) exhibits the dense PBs of sample DF2273, which evidences the occurrence of phase transformations after deformation at 2273 K.

TEM observation was conducted on the sample DF2273 to further reveal the microstructure evolution after deformation at 2273 K, and the results were presented in Fig. 9. Fig. 9(a–c) shows the DF image, elemental distribution, and SAED pattern in the BCC phase, respectively. Ta- and C-rich rod-shaped precipitation appears on the BCC matrix, which can be identified as the FCC phase by the SAED pattern at PB. As indicated by the white arrows in Fig. 9(b), the enrichment of Ta at the end of the rods implies that the formation of FCC precipitation may be related to the segregation of Ta. Besides, there is an obvious parallel relationship between the FCC precipitation with the BCC matrix, as evidenced by the SAED pattern at the PB in Fig. 9(c). Dense dislocations are assembled around the FCC precipitation, as shown in Fig. 9(d), which

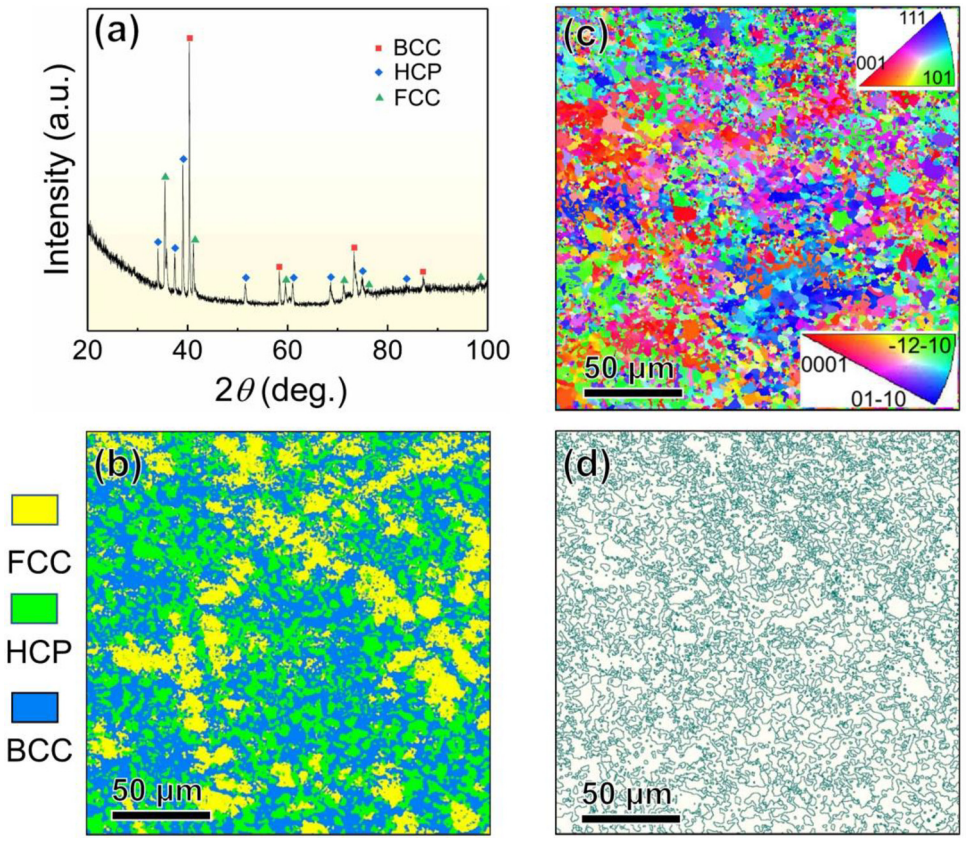

Fig. 8. Microstructure of the sample DF2273. (a) XRD pattern; (b) phase distribution; (c) orientation map; (d) phase boundary distribution.

implies that dislocation slip plays a significant role in the formation of the FCC precipitation. For the FCC phase, mechanical twins together with SFs are observed in Fig. 9(e), as indicated by the blue and yellow arrows, respectively. Notably, the SFs density in the FCC phase of the sample DF2273 is significantly reduced compared with that of the sample AC. As shown in Fig. 9(g), the mechanical twin initiates at the intersecting SFs and grows up towards the insider of the FCC grain, which indicates that the deformation of the FCC phase is dominated by the movement of SFs and twinning. Meanwhile, more TBs generate at the close-packed planes, i.e., $\{111\}_{FCC}$ planes, along with the movement of the original TBs, which greatly contributes to the deformation of FCC grains, as shown in Fig. 9(h). Fig. 9(h, i) shows that the BCC phase precipitates on TBs, which implies that phase transformation also contributes to the deformation of FCC grains during compression. For the HCP phase, both basal slip and cross-slip are observed (Fig. 9(j, k)), and BCC grains precipitate along the dislocations (Fig. 9(k)). As mentioned above, all the triple phases are metastable during the deformation at 2273 K.

4. Discussion

4.1. Metastability of the $W_{20}Ta_{30}Mo_{20}C_{30}$ RHEC

The phase transformations occurring at 2273 K are irrespective of deformation, revealing the microstructure of $W_{20}Ta_{30}Mo_{20}C_{30}$ RHEC is metastable at 2273 K. The structural metastability of $W_{20}Ta_{30}Mo_{20}C_{30}$ RHEC may be related to the complex solidification process and the multi-principal effect [28]. The equilibrium phase diagram shows complex phase transformations (Fig. 3(a)), but only large FCC dendrites, HCP matrix, eutectic structure, and a small amount of eutectoid structure, corresponding to LS-1, LS-3, LS-4, and SS-6, respectively, can be observed (Fig. 4). This suggests that some of the phase transformation stages are not sufficiently carried out, as simulated by the Scheil solidification in Fig. 3(c). At LS-2, for example, the FCC dendrites with large grain sizes are difficult to diffuse back into the liquid to form the HCP phase due to the high solidification rate, narrow temperature range of phase transformation, and high cohesive energy of the ceramic phase. In addition, the solid-state phase transformations result in the conversion of the HCP or FCC ceramic phases to the BCC solid solution, as shown in SS-5 to SS-7 in Table 1. Elemental diffusion is required in the decomposition of the HCP ceramic phase into the BCC solid solution with the FCC ceramic phase, thereby only a small amount of eutectoid structure can be found at the PBs between the FCC dendrites and HCP matrix, as shown in Fig. 4(i). Since both the multi-principal solid solution and ceramic phases have low atomic diffusion rates, SS-5 and SS-7 are more likely displacive transformations rather than diffusion transformations. As shown in Fig. 10(a), the BCC phase precipitates in the FCC dendrites, which is consistent with SS-7. Fig. 10(b, c) exhibits the orientation relationship between the BCC phase ($\{110\}<\bar{1}11>$) with the FCC phase ($\{111\}<\bar{1}10>$) and the HCP phase ($\{0001\}<11\bar{2}0>$), respectively, and the distribution of misorientation deviation is presented in Fig. 10(d). It is obvious that the BCC–HCP orientation relationship is widely distributed between 0°–40° and the highest frequency of 24.2% is obtained at 39.5°, while the BCC-FCC orientation relationship is mainly concentrated at 42.5° which reaches 94.9%. This suggests that BCC–HCP PBs can be obtained by both diffusion transformation (LS-4 and SS-6) and displacive transformation (SS-5) while BCC-FCC PBs are mainly obtained by the latter (SS-7). Both insufficient phase transformation and displacive transforma-

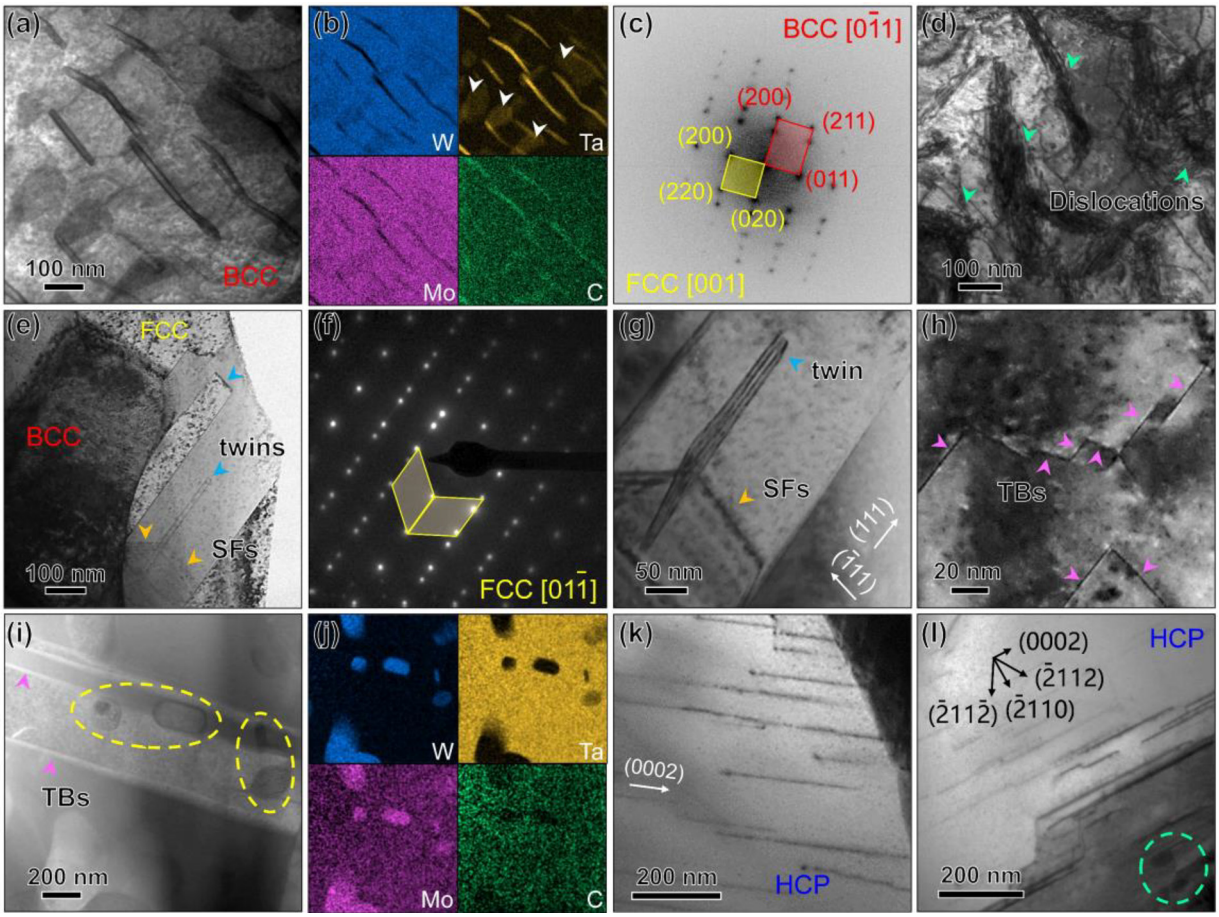

Fig. 9. TEM analysis of the sample DF2273. (a) DF image, (b) elemental mapping, (c) SAED pattern, and (d) the interaction between FCC precipitation with dislocations in the BCC phase; (e) BF image and (f) SAED pattern of the FCC phase; (g, h) enlarged views of (e); (i) BCC phase precipitated at the TBs; (j) elemental maps of image (i); (k) planar slip and (l) cross slip of dislocations in the HCP phase.

tion bring great metastability to the $W_{20}Ta_{30}Mo_{20}C_{30}$ RHEC [29]. Consequently, phase transformations occurred during the annealing treatment at 2273 K. Additionally, both the non-equilibrium solidification and complex phase transformations lead to supersaturated composition in the multicomponent solid solution or ceramic phases, which further enhances the structural metastability of the RHEC.

4.2. The effects of temperature and stress on the microstructure

The insufficient and solid-state phase transformations result in severe lattice distortion in sample AC, as evidenced by the large local strain and the high density of GNDs in Fig. 1(f). After annealing, both the content and thickness of the eutectoid structure increase (Fig. 7(h)), while the BCC phase precipitates in the FCC dendrites as shown in both Figs. 6(b) and 7(a). Apparently, the uncompleted solid-state phase transformations are promoted and the supersaturated phases decompose, which is driven by the combination of ultrahigh temperature and high-density solidification defects. The aggravated volume change caused by thermal process and phase transformations can further promote the shear deformation of ceramic phases. Therefore, the FCC phase, which was difficult to be deformed by dislocation slip, must accommodate the volume change by twinning.

Compared with sample UDF2273, more phase transformations occurred after the deformation at 2273 K, suggesting the additional stress further enhances the metastability of $W_{20}Ta_{30}Mo_{20}C_{30}$ RHEC. Though the precipitation behavior appeared in all the triple phases, their triggered mechanisms are different. As multiple slip systems can be easily motivated at elevated temperatures, cross-slip, and dislocation multiplication would be greatly enhanced during the deformation of the BCC solid solution. Notably, the cohesive energy between the atoms C with Ta is significantly higher than that between C with W and Mo [30], which leads to the selective dislocation slip in the BCC phase. It suggests that more C and Ta atoms segregated together to gradually form the Ta-C-rich region, and finally precipitated as the FCC phase. This mechanism, whereby elements segregate along with the dislocation movement and eventually lead to phase decomposition, has been demonstrated in the carbides of Ni-based superalloys [31]. Besides, the motivation of the multiple slip systems in the BCC phase also determines the appearance of the FCC precipitation. On the one hand, the FCC phase can grow up to rod-shaped precipitation by pinning dislocations along the same orientation, as shown in Fig. 9(d). On the other hand, the dislocations can also be pinned up through different slip systems, which allows FCC precipitation to grow up in another orientation, as indicated by the white arrows in Fig. 9(b). The decomposition of the BCC phase can significantly reduce the lattice distortion and then produce abundant semi-coherent PBs with low interfacial energy, the FCC phase can continuously precipitate in the BCC phase during the deformation at 2273 K.

Compared with the BCC solid solution, stronger cohesive energy is present in the HCP ceramic phase due to the higher content of C, but precipitation still occurs along dislocations, as shown in Fig. 9(l). Notably, the precipitated phase tends to appear in the region with abundant prismatic and pyramidal dislocations rather

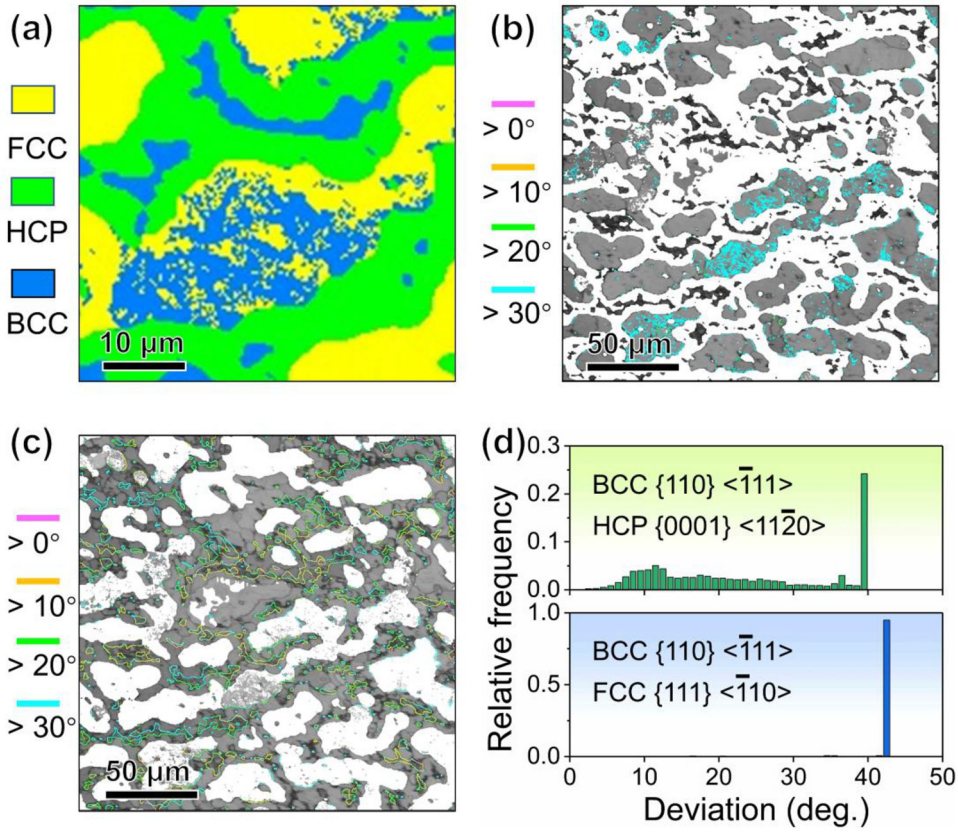

Fig. 10. EBSD analysis of PBs in the sample AC. (a) enlarged view at the red square of Fig. 1(d); orientation relationship between (b) the FCC and BCC phases, (c) the HCP and BCC phase; (d) deviation distribution of PBs.

than where there are dense basal dislocations, as illustrated in Fig. 9(k, l), respectively, suggesting that the activation of cross slip is crucial for the precipitation in the HCP phase. It reveals less reaction between basal dislocations and C element and evidence that the long-period ordered structure in the HCP phase is mainly located at prismatic and pyramidal planes rather than basal planes. Moreover, the appearance of the dislocation cross slip indicates that the plastic deformation ability of the HCP ceramic phase is improved as deformed at 2273 K [32].

The precipitation behavior in the FCC phase is different from that in the BCC and HCP phases. Dense dislocations are observed in the BCC and HCP phases after the deformation at 2273 K, as shown in Fig. 9(d, k, l). However, only a small amount of SFs are detected and dislocations are invisible in the FCC phase of sample DF2273, whereas mechanical twins can be found. Notably, a small number of dislocations and a high density of SFs can be observed in the FCC phase of sample AC. The insufficient deformation ability of the FCC phase at 2273 K makes the FCC grains need to deform by twinning. The mechanical twins can reduce the mean free path of dislocations and thereby inhibit the activation and motion of dislocations (so-called “dynamic Hall-Petch effect”) [33]. Notably, twinning activity in the FCC phase is strongly grain-size dependent and usually diminishes as the grain size decreases [34]. However, in this work, both annealing twins and mechanical twins were present in submicron-scale or nanoscale FCC grains, demonstrating the multi-component composition and high content of C favors the activation of twinning in ultrafine grains [35,36]. The absence of dislocations hinders elemental segregation, resulting in the inability to precipitate inside the FCC grains. Therefore, the BCC precipitation nucleates at TBs of the FCC grains, which accommodates additional plastic deformation and helps to restrain cracks.

Taken together, the deformation mechanisms of the RHEC at 2273 K are mainly dislocation-glide-dominated with transformation-induced plasticity for the BCC and HCP phases, while twinning- and transformation-induced plasticity for the FCC phase.

4.3. The effects of the structural metastability on the ultrahigh-temperature mechanical properties

The introduction of the high-content C (30 at.%) plays an important role in obtaining excellent yield strength and specific yield strength at ultrahigh temperatures for $W_{20}Ta_{30}Mo_{20}C_{30}$ RHEC. This not only significantly reduces the density of RHEC, but also allows the formation of a high fraction of metastable ceramic phases (~90%) at the as-cast state, which is conducive to resisting plastic deformation at the early stage of compression.

The stress-strain behavior can be correlated with the microstructural evolution during the deformation at 2273 K. Firstly, compared samples UDF2273 with AC, ultrahigh temperature promotes the incomplete solid-state phase transformations, which significantly refines the grain size of all triple phases. Secondly, these phase transformations (i.e., ceramic phases and solid solution precipitated from each other) produce a high density of additional PBs, which leads to an enhanced hardening effect. Thirdly, the existence of C strengthens the GBs and thus helps to resist grain sliding [11,37]. Compared with the sample UDF2273, additional phase transformations were triggered as the RHEC deformed at 2273 K owing to the structural metastability. It should be noted

that the strain softening induced by dynamic recrystallization is usually persistent in many RHEAs [38–40]. It is the formation of a high density of semi-coherent PBs and a large number of mechanical twins that inhibits the persistent strain softening after a stress drop of ~80 MPa.

$W_{20}Ta_{30}Mo_{20}C_{30}$ RHEC also shows exceptional plasticity at 2273 K without fracture as straining of ~40%. One reason is that grain refinement in triple phases avoids preferential initiation of cracks in large-size ceramic phases [14]. Another reason is that dislocation slip, twinning, and phase transformation concurrently contribute to plasticity, which may be unique to RHECs with high C content.

5. Conclusions

In this work, a $W_{20}Ta_{30}Mo_{20}C_{30}$ (at.%) refractory high-entropy composite (RHEC) was prepared by vacuum arc melting and the microstructure of the as-cast, undeformed (annealed) at 2273 K and compressed at 2273 K were studied by TEM. The as-cast RHEC was composed of FCC dendrites, HCP matrix, HCP-BCC eutectic structure, and FCC-BCC eutectoid structure, and exhibited high-density defects owing to the complex phase transformations during solidification. At 2273 K, the FCC and HCP ceramic phases showed higher metastability than the BCC solid solution. Annealing treatment at 2273 K promoted the BCC phase precipitation in the FCC dendrites and the decomposition of the HCP phase into the FCC-BCC eutectoid structure, which leads to significant grain refinement of all triple phases. During the compression at 2273 K, ceramic phases and solid solution precipitated out from each other, which is conducive to avoiding persistent softening after the RHEC yielding. $W_{20}Ta_{30}Mo_{20}C_{30}$ RHEC shows outstanding specific yield strength at both 1873 and 2273 K compared with other RHEAs/RHECs, which is mainly attributed to the high-fraction ceramic phases and high-density PBs. Further analyses suggested that the dominant deformation mechanisms were dislocation slide and transformation-induced plasticity in the BCC and HCP phases while twinning- and transformation-induced plasticity in the FCC phase. To our best knowledge, this work reports the mechanical properties and microstructure evolution at 2273 K for the first time among the RHEAs and RHECs. These findings provide a novel strategy for designing RHECs through alloying high-content nonmetallic elements, which helps to further break through the performance limit at ultrahigh temperatures and lighten the refractory materials (both beneficial for their applications).

Declaration of Competing Interest

The authors declare that they have no known competing financial interests or personal relationships that could have appeared to influence the work reported in this paper.

Acknowledgments

This work is supported by the National Key Research and Development Program of China (Grant No. 2018YFC1902400), the National Natural Science Foundation of China (Grant No. 51975582), the Key Research and Development Program of Jiangsu Province (Grant No. BE2021088).

Supplementary materials

Supplementary material associated with this article can be found, in the online version, at doi:10.1016/j.jmst.2023.05.014.

Reference

[1] D.B. Miracle, O.N. Senkov, Acta Mater. 122 (2017) 448–511.
[2] W. Xiong, A.X.Y. Guo, S. Zhan, C. Liu, S.C. Cao, J. Mater. Sci. Technol. 142 (2023) 196–215.
[3] P. Tsakiropoulos, Prog. Mater. Sci. 123 (2022) 100714.
[4] J.H. Perepezko, Science 326 (2009) 1068–1069.
[5] O.N. Senkov, G.B. Wilks, D.B. Miracle, C.P. Chuang, P.K. Liaw, Intermetallics 18 (2010) 1758–1765.
[6] O.N. Senkov, G.B. Wilks, J.M. Scott, D.B. Miracle, Intermetallics 19 (2011) 698–706.
[7] O.N. Senkov, D.B. Miracle, K.J. Chaput, J. Couzinie, J. Mater. Res. 33 (2018) 3092–3128.
[8] Z.D. Han, N. Chen, S.F. Zhao, L.W. Fan, G.N. Yang, Y. Shao, K.F. Yao, Intermetallics 84 (2017) 153–157.
[9] Y. Wan, J. Mo, X. Wang, Z. Zhang, B. Shen, X. Liang, Acta Metall. Sin.-Engl. Lett. 34 (2021) 1585–1590.
[10] Y. Wan, Q. Wang, J. Mo, Z. Zhang, X. Wang, X. Liang, B. Shen, Adv. Eng. Mater. 24 (2022) 2100765.
[11] Z. Wang, H. Wu, Y. Wu, H. Huang, X. Zhu, Y. Zhang, H. Zhu, X. Yuan, Q. Chen, S. Wang, X. Liu, H. Wang, S. Jiang, M.J. Kim, Z. Lu, Mater. Today 54 (2022) 83–89.
[12] Y. Wan, X. Wang, Z. Zhang, J. Mo, B. Shen, X. Liang, J. Alloy. Compd. 889 (2021) 161645.
[13] S. Wu, D. Qiao, H. Zhang, J. Miao, H. Zhao, J. Wang, Y. Lu, T. Wang, T. Li, J. Mater. Sci. Technol. 97 (2022) 229–238.
[14] B. Wang, Q. Wang, B. Sun, J. Mo, Y. Guo, X. Liang, B. Shen, J. Mater. Sci. Technol. 149 (2023) 31–41.
[15] Q. Wei, X. Xu, Q. Shen, G. Luo, J. Zhang, J. Li, Q. Fang, C.T. Liu, M. Chen, T.G. Nieh, J. Chen, Sci. Adv. 8 (2022) eabo2068.
[16] T.R. Middya, A.N. Basu, S. Sengupta, J. Appl. Phys. 58 (1985) 1809–1813.
[17] H. Mao, H. Chen, Q. Chen, J. Phase Equilib. Diff. 38 (2017) 353–368.
[18] T. Li, S. Wang, W. Fan, Y. Lu, T. Wang, T. Li, P.K. Liaw, Acta Mater. 246 (2023) 118728.
[19] Z. Wang, W. Lu, H. Zhao, C.H. Liebscher, J. He, D. Ponge, D. Raabe, Z. Li, Sci. Adv. 6 (2020) eaba9543.
[20] Y. Mu, L. He, S. Deng, Y. Jia, Y. Jia, G. Wang, Q. Zhai, P.K. Liaw, C. Liu, Acta Mater. 232 (2022) 117975.
[21] B.L. Bramfitt, Metall. Mater. Trans. B 1 (1970) 2958.
[22] L. Vegard, Z. Med. Phys. 5 (1921) 17–26.
[23] S. Wu, D. Qiao, H. Zhao, J. Wang, Y. Lu, J. Alloy. Compd. 889 (2021) 161800.
[24] C. Juan, M. Tsai, C. Tsai, C. Lin, W. Wang, C. Yang, S. Chen, S. Lin, J. Yeh, Intermetallics 62 (2015) 76–83.
[25] O.N. Senkov, J.M. Scott, S.V. Senkova, F. Meisenkothen, D.B. Miracle, C.F. Woodward, J. Mater. Sci. 47 (2012) 4062–4074.
[26] M. Wang, Z. Ma, Z. Xu, X. Cheng, J. Alloy. Compd. 803 (2019) 778–785.
[27] X.W. Nie, M.D. Cai, S. Cai, Int. J. Refract. Met. H. 98 (2021) 105568.
[28] J. Yeh, Ann. Chim.-Sci. Mat. 31 (2006) 633–648.
[29] W. Li, D. Xie, D. Li, Y. Zhang, Y. Gao, P.K. Liaw, Prog. Mater. Sci. 108 (2021) 111777.
[30] A. Takeuchi, A. Inoue, Mater. Trans. 46 (2005) 2817–2829.
[31] H. Ge, G. Liu, S. Zheng, Y. Yang, K. Liu, X. Ma, Acta Mater. 246 (2023) 118669.
[32] X. Wen, H. Huang, H. Wu, M. Zhou, Y. Bu, X. Yuan, S. Jiang, H. Wang, X. Liu, H. Wang, J. Liu, Y. Wu, Z. Lu, J. Mater. Sci. Technol. 134 (2023) 1–10.
[33] Z. Wu, H. Bei, G.M. Pharr, E.P. George, Acta Mater. 81 (2014) 428–441.
[34] I. Gutierrez-Urrutia, S. Zaefferer, D. Raabe, Mater. Sci. Eng., A 527 (2010) 3552–3560.
[35] N.D. Stepanov, D.G. Shaysultanov, R.S. Chernichenko, N.Y. Yurchenko, S.V. Zherebtsov, M.A. Tikhonovsky, G.A. Salishchev, J. Alloy. Compd. 693 (2017) 394–405.
[36] L.B. Chen, R. Wei, K. Tang, J. Zhang, F. Jiang, L. He, J. Sun, Mater. Sci. Eng. A 716 (2018) 150–156.
[37] T. Li, J. Miao, Y. Lu, T. Wang, T. Li, Int. J. Refract. Met. Hard Mat. 103 (2022) 105762.
[38] R.R. Eleti, T. Bhattacharjee, A. Shibata, N. Tsuji, Acta Mater. 171 (2019) 132–145.
[39] R.R. Eleti, A.H. Chokshi, A. Shibata, N. Tsuji, Acta Mater. 183 (2020) 64–77.
[40] T. Li, Y. Lu, Z. Li, T. Wang, T. Li, Intermetallics 146 (2022) 107586.